Journal of Materials Chemistry A

Accepted Manuscript

ROYAL SOCIETY OF CHEMISTRY

www.rsc.org/materialsA

Layer-by-Layer of nitrogen-doped graphene quantum dots monolayer decorated one-dimensional semiconductor nanoarchitectures for solar-driven water splitting

Zhiping Zeng, Fang-Xing Xiao*, Xuchun Gui, Rong Wang, Bin Liu*, Timothy Thatt Yang Tan*

Dr. Z. Zeng, Dr. F. X. Xiao, Prof B. Liu, Prof. T. T. Y. Tan
School of Chemical and Biomedical Engineering
Nanyang Technological University
Singapore 639798, Singapore
E-mail: fangxing2010@gmail.com (F. X. Xiao), liubin@ntu.edu.sg (B. Liu), tytan@ntu.edu.sg (T. T. Y. Tan)
Dr. Z. Zeng, Prof. R. Wang
Singapore Membrane Technology Center
Nanyang Environment and Water Research Institute
Interdisciplinary Graduate School
Nanyang Technological University
Singapore 637141, Singapore
Prof. X. Gui
State Key Lab of Optoelectronic Materials and Technologies
School of Electronics and Information Technology
Sun Yat-sen University, Guangzhou 510275, China

Table of Contents

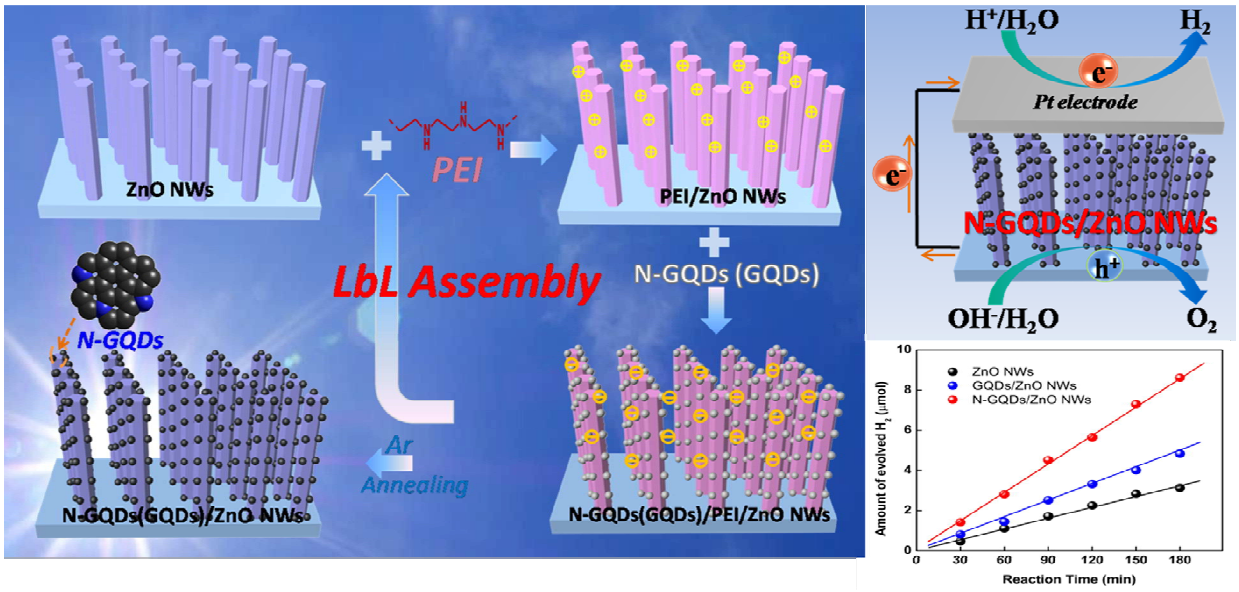

Abstract

A layer-by-layer (LbL) assembly of highly ordered nitrogen-doped graphene quantum dots (N-GQDs)/ZnO nanowires (NWs) heterostructures was demonstrated as a high performance photoanode in photoelectrochemical (PEC) hydrogen generation for the first time. The nitrogen doping of GQDs was achieved by a facile synthetic strategy under ambient conditions, based on which, N-GQDs were uniformly and intimately deposited on the ZnO NWs framework *via* pronounced electrostatic interaction. The deposited amount of N-GQDs and PEC water splitting performances of N-GQDs/one-dimensional (1D) semiconductor heterostructures can be tuned by assembly layer. The integrative roles of nitrogen doping and photosensitization of GQDs in conjunction with intimate interfacial integration between the photoanode components afforded by the LbL assembly strategy were found to collaboratively contribute to enhanced PEC water splitting. It is anticipated that our work could afford a facile and general strategy for steering toward the rational design of a large variety of N-GQDs/1D semiconductor nanoarchitectures for extensive photocatalytic or PEC applications.

KEYWORDS: Nitrogen Doping, Graphene Quantum Dots, ZnO Nanowires, Layer-by-Layer, Photoelectrochemical Water Splitting.

1. Introduction

Harvesting sunlight to produce hydrogen fuel remains one of the central challenges for solving global energy crisis.[1-6] Photoelectrochemical (PEC) cells for solar hydrogen production, as a green and promising approach to provide clean energy, have attracted enormous attention since the pioneer work reported by Fujishima and Honda in 1972.[3,7] Thus far, a large variety of nanostructured metal oxides have been explored as photoelectrodes for PEC water splitting, among which one-dimensional (1D) semiconductors have been deemed as one of promising

electrodes for PEC cells due to their intrinsic structural advantages in comparison with bulk counterparts, such as fast and long-distance electron transport, larger surface area and pore volume, and enhanced light absorption and scattering capabilities.[8-11] In particular, 1D zinc oxide (ZnO) nanostructures directly growing on conducting substrates have been extensively utilized for PEC applications due to high electron mobility, environmental friendliness, and comparable PEC and photocatalytic performances to TiO_2.[12,13] Nevertheless, owing to its relatively large bandgap (*ca.* 3.2 eV), ZnO only absorbs ultraviolet light which accounts for merely 4-5 % of solar spectrum.[14] Therefore, it is highly desirable to extend light absorption of ZnO to visible region for substantial solar energy utilization.

Diverse strategies have been developed to fabricate various 1D ZnO-based hybrid nanostructures for PEC water splitting under simulated solar light or visible light irradiation, such as noble metal deposition (*e.g.*, Au, Ag, and Pt),[15-18] transition metal ions doping or non-metal elemental atoms doping,[19-22] sensitization with narrow-band-gap semiconductors (*e.g.*, CdS, CdSe, CdTe, and PbS quantum dots),[23] or formation of nanostructured heterostructures with secondary semiconductors.[24] Despite these endeavors, constructing well-defined 1D ZnO-based composite heterostructures with pronounced light absorption especially in visible region along with efficient separation of photogenerated electron-hole pairs continues to be challenging.

As a new member of carbon materials, graphene quantum dots (GQDs) composed of strong sp^2-bonded carbon have garnered increasing research interest because of its analogous semiconductor properties with tunable bandgap which can be tailored by size modulation and chemical selective doping.[25-33] In spite of the fascinating physical-co-chemical properties of GQDs, reports on rational design of GQDs/semiconductor nanocomposites are still rare. Note that synthetic approaches for fabricating GQDs/semiconductor nanocomposites in previous work

are relatively complicated, and environmentally-unfriendly, and tunable control over GQDs deposition is still far from satisfactory.[34] Moreover, intimate integration of GQDs and semiconductors at the nanoscale level *via* conventional approach is hard to achieve, which is of paramount importance to interfacial charge carrier transport. On the other hand, it has been well-established that electrical conductivity of GQDs and charge-transfer as well as electrolyte-electrode interactions can be significantly improved by nitrogen doping in graphene frame,[35,36] which is in favor of catalyzing water-splitting under visible light irradiation. Although nitrogen-doped graphene have been explored in various fields, such as fuel cells,[37] lithium ion batteries,[38] and supercapacitors,[39] until now, the construction of well-defined N-GQDs/semiconductor heterostructures through a facile, green, and easily accessible synthetic strategy for PEC hydrogen production has not yet be reported.

Layer-by-Layer (LbL) assembly technique, as one of promising bottom-up fabrication strategies, demonstrates remarkable advantages compared with conventional approaches in terms of simplicity and versatility, which furnishes tunable control over micro-structure, thickness, and composition of the assemblies.[40-43] Particularly, intrinsic negatively charged surface and hydrophility of N-GQDs renders it a suitable building block for LbL assembly on the hydrophilic surface of ZnO NWs based on electrostatic interaction, thereby resulting in a tailorable nano-architecture. Herein, a facile and green LbL assembly approach has been developed to construct highly ordered N-GQDs/ZnO NWs heterostructures based on substantial electrostatic interaction, in which N-GQDs prepared by a facile synthetic strategy, was used as a predominant building block for LbL assembly on the ZnO NWs framework. Moreover, it was found that the LbL-assembled N-GQDs/ZnO NWs heterostructures exhibit significantly enhanced PEC water splitting performances under both simulated solar and visible light irradiation. Furthermore, the

deposition amount of N-GQDs on the scaffold of ZnO NWs can be easily tuned by assembly layer. The contributing role of N-GQDs was clearly defined and the PEC mechanism of N-GQDs/ZnO NWs heterostructures was specifically discussed. It is hoped that the current work could provide a new synthetic strategy for the rational fabrication of N-GQDs/semiconductor nanoarchitectures and, more significantly, afford new insights for the potential applications of N-GQDs in the field of photocatalysis or PEC water splitting.

2. Results and discussion

2.1 Synthesis and characterization of N-GQDs

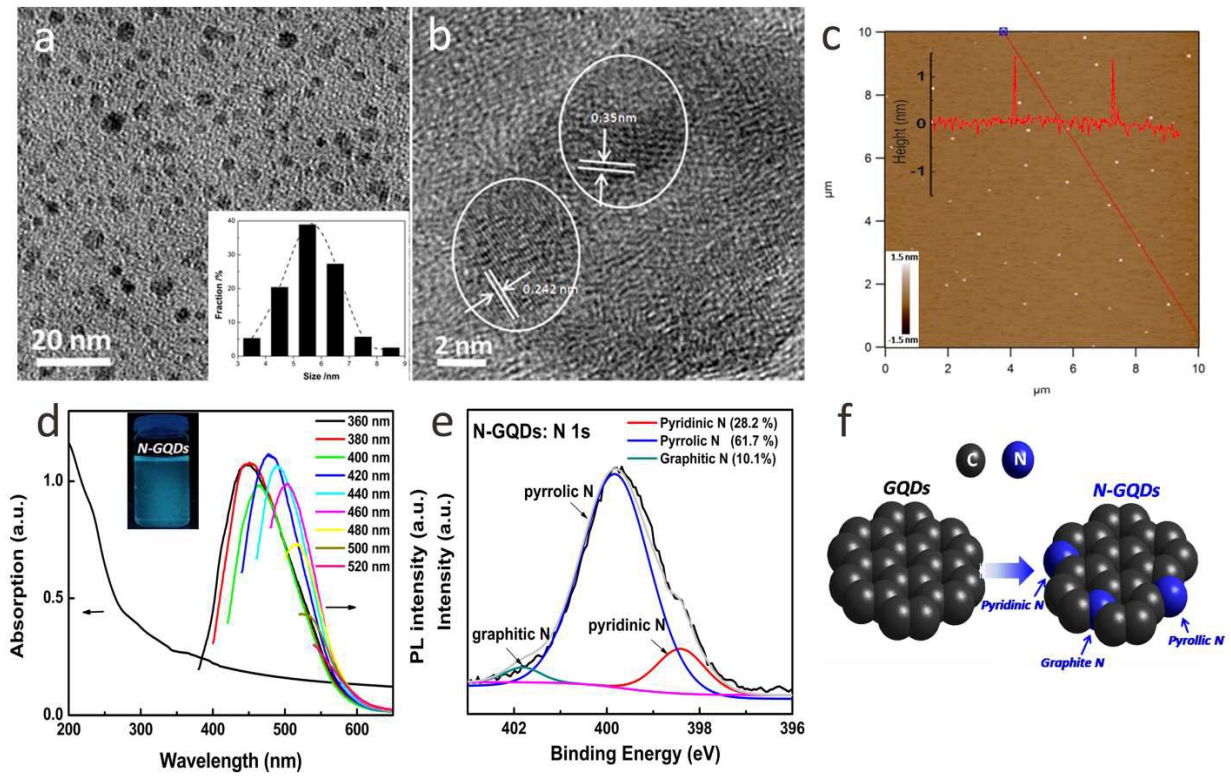

Fig. 1 (a) TEM image of N-GQDs with size distribution histogram in the inset, (b) high-resolution TEM (HRTEM) image of N-GQDs, (c) AFM image of N-GQDs with corresponding height profile in the inset, (d) UV-vis absorption spectrum and photoluminescence spectra of N-GQDs with photoexcited digital graph (365 nm UV light) in the inset, (e) high-resolution N 1s XPS spectrum of N-GQDs, and (f) schematic illustration of N-GQDs with different types of doped nitrogen atoms.

A transmission electron microscopy (TEM) image (**Fig. 1a**) depicts that N-GQDs possess uniform size ranging from 3 to 9 nm with mean particle size of 5.8 nm (inset of **Fig. 1a**). **Fig. 1b** shows the high-resolution TEM (HRTEM) of N-GQDs in which lattice-fringe spacing were determined to be *ca.* 0.242 and 0.35 nm, which correspond well to (1120) and (002) crystal planes of graphite,[30,44,45] respectively. Undoped GQDs also exhibit uniform size of around 5.6 nm (**Fig. S1a**), implying the particle size of GQDs was barely changed with nitrogen doping. Moreover, as shown in **Fig. 1c**, atomic force microscope (AFM) was utilized to probe the morphology and height of N-GQDs**,** of which the height profile was determined to be *ca.* 1.0-1.5 nm, strongly suggesting that N-GQDs consisted of 1-2 graphene layers inherited from GQDs precursor. This conclusion can be corroborated by the AFM result of GQDs (**Fig. S1b**) which exhibits analogous topographic height profile ranging from 0.7 to 1.2 nm. Noteworthily, although UV-vis absorption spectrum of N-GQDs (**Fig. 1d**) displays similar light absorption to GQDs (**Fig. S2**) with two characteristic absorption bands at 240 and 350 nm attributed to the quantum confinement effect, N-GQDs exhibit substantially enhanced absorption in visible region which can be ascribed to the nitrogen doping. Furthermore, as displayed in the inset of **Fig. 1d**, an obvious blue luminescence was observed over N-GQDs when it was irradiated with UV light (365 nm) which is in agreement with the photoluminescence feature of N-GQDs. The PL emission band of N-GQDs can be tuned by exciting light wavelength ranging from 360 to 520 nm, indicating an unique optoelectronic property due to large defects amount and high conductivity of nitrogen-doping of GQDs.[45] Fourier transform infrared spectroscopy (FTIR) characterization (**Fig. S3**) depicts the typical peak of GQDs at 1712 cm^{-1}, corresponding to carbonyl and carboxylic acid groups. However, the peak decreases after nitrogen doping, suggesting that carbonyl and carboxylic functional groups of GQDs are involved in the

intermolecular dehydrolysis reaction between neighboring carbonyl/carboxyl and amine groups to form pyrrolic *N* in GQDs.[45] Notably, a new peak at 1577 cm^{-1} was clearly observed in the FTIR spectrum of N-GQDs, which is attributed to C=N bond in N-GQDs, thus indicating nitrogen has been successfully doped in the GQDs frame.[35] As shown in **Fig. S4**, N-GQDs exhibit larger I_D/I_G in the Raman results ratio than GQDs which is mainly due to the introduction of defects and formation of different bond lengths between C-C and C-N bonds afforded by nitrogen doping.[46,47]

Survey X-ray photoelectron spectroscopy (XPS) spectrum of N-GQDs is displayed in **Fig. S5a**, which reveals that N-GQDs consist mainly of C, N, and O core-elements. More specifically, high-resolution C 1s spectrum of N-GQDs (**Fig. S5b**) can be deconvoluted to four Gaussian peaks located at 284.6, 286.13, 287.2 and 288.08 eV, corresponding to the C-C/C-H, C-OH, C-N, and O=C-OH bonds, respectively.[27,48] Consistently, high-resolution N 1s spectrum of N-GQDs, as shown in **Fig. 1e**, can be deconvoluted predominantly to three peaks at 398.3, 399.8 and 401.8 eV, which correspond to pyridine, pyrrolic and graphitic nitrogen atoms, respectively.[27,45] Moreover, percentage of nitrogen atoms doped in the N-GQDs was determined to be *ca.* 5.4 at. % based on XPS result, which is comparable to values reported by other synthetic approaches, such as annealing with NH_3 atmosphere[46,48] or microware plasma-assisted chemical vapor deposition method.[49,50] The result indicates that our synthetic method is effective in preparing N-GQDs with favorable nitrogen doping level. In addition, atomic ratios of C 1s to O 1s (C/O) in N-GQDs and GQDs were determined to be 3.28 and 1.24, indicating GQDs were partially reducted during the nitrogen doping process. Consequently, XPS results suggest that nitrogen-doping and partial reduction of GQDs occurred simultaneously, which would facilitate

restoring the electron conductivity of GQDs. For clarification, different types of C-N bonds in N-GQDs were depicted in **Fig. 1f**.

2.2 LbL assembly of N-GQDs/ZnO NWs heterostructures

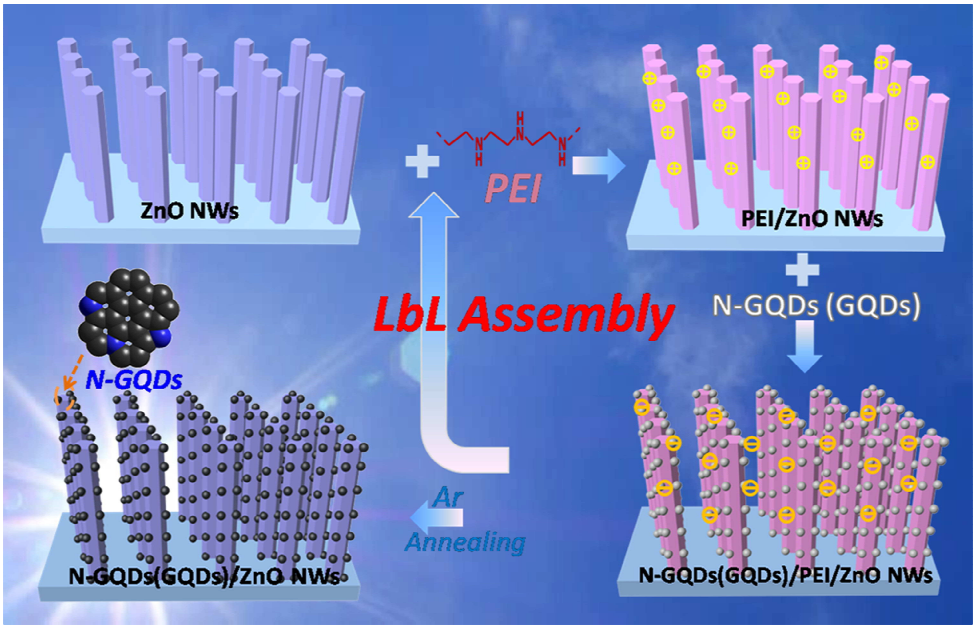

Fig. 2 Schematic illustration for LbL assembly of N-GQDs (or GQDs) decorated ZnO nanowires arrays (N-GQDs (or GQDs)/ZnO NWs) heterostructures.

Fig. 2 depicts the process for LbL assembly of N-GQDs (or GQDs)/ZnO NWs heterostructure. Specifically, single-crystalline ZnO NWs grown vertically from fluorine-doped tin oxide (FTO) substrate were firstly synthesized by a hydrothermal method. Subsequently, ZnO NWs scaffold after calcination was modified with polyethylenimine (PEI) which affords a positively charged surface. PEI has the unique feature of the presence of amine groups which endows it with high affinity to the hydrophilic ZnO NWs surface (**Fig. S6**).[51] Based on which, negatively charged N-GQDs or GQDs (**Fig. S7**) can be spontaneously and uniformly assembled on the ZnO NWs substrate *via* substantial electrostatic interaction, thereby giving rise to well-defined N-GQDs/ZnO (or GQDs/ZnO) NWs heterostructure with one deposition cycle of N-GQDs (or GQDs). Then, by the same way, the thus-attained N-GQDs/ZnO (or GQDs/ZnO) NWs

heterostructure was re-treated with PEI and assembled with N-GQDs (or GQDs), by which deposition amount of N-GQDs or GQDs on ZnO NWs was tuned by assembly cycle. Analogous to ZnO NWs, other 1D semiconductors such as TiO_2 nanorod (NRs) can also be modified with N-GQDs or GQDs through the same LbL assembly strategy to fabricate N-GQDs (or GQDs)/TiO_2 NRs heterostructures. Finally, these LbL-assembled N-GQDs (or GQDs)/1D semiconductor (ZnO NWs or TiO_2 NRs) nanoarchitectures were calcined in an argon atmosphere to completely remove PEI moiety and, simultaneously, to achieve reduction of N-GQDs (or GQDs), which is beneficial for restoring electron conductivity of N-GQDs (or GQDs) and achieving more intimate interfacial contact between N-GQDs (or GQDs) component and 1D semiconductors scaffold.

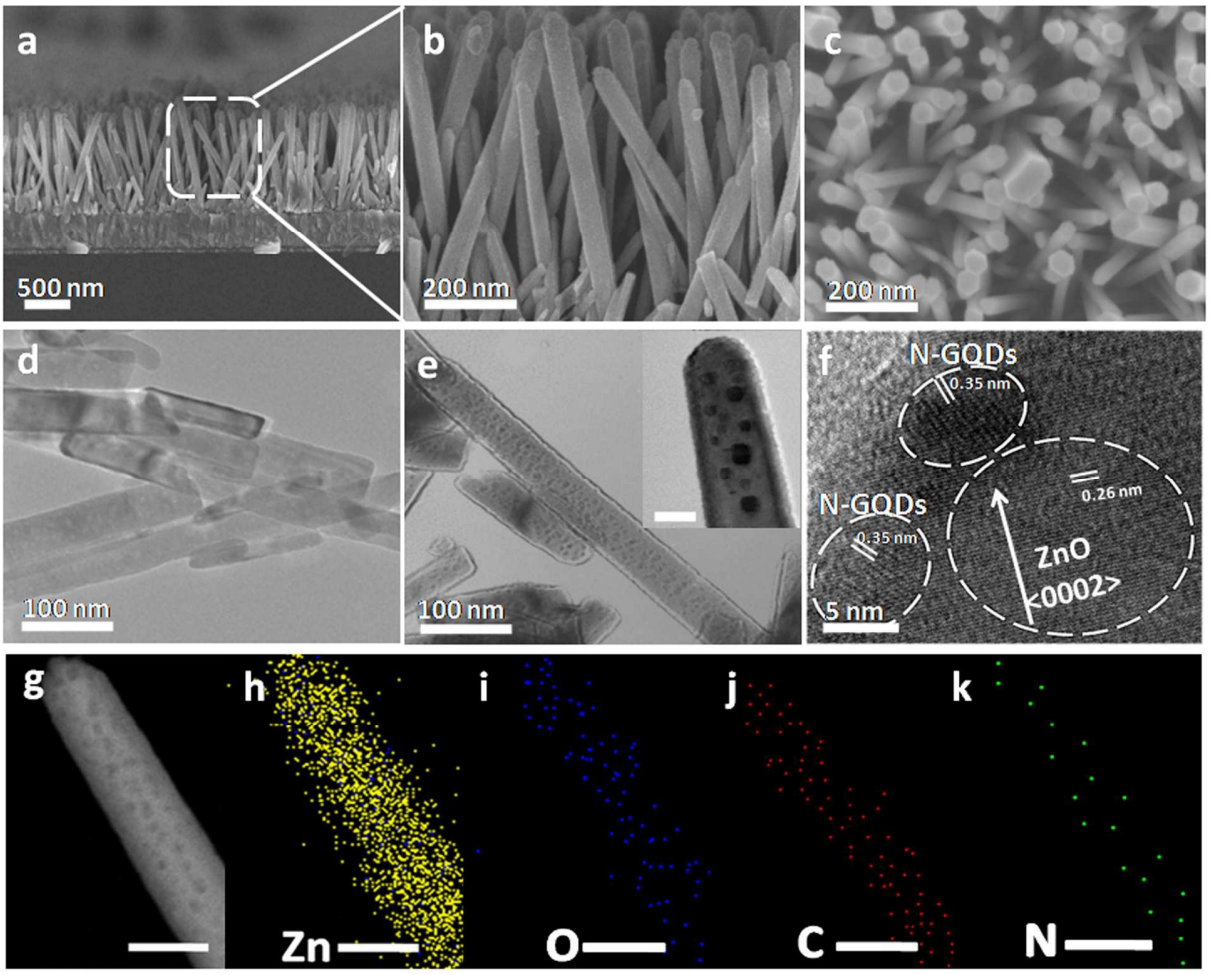

Fig. 3 Cross-sectional (a & b) and (c) top-view FESEM images of N-GQDs/ZnO NWs heterostructure (one assembly layer), (d) TEM image of ZnO NWs, (e) TEM image of N-GQDs/ZnO NWs heterostructure with high-magnification image in the inset (scale bar: 20 nm), (f) HRTEM image of N-GQDs/ZnO NWs heterostructure, and (g) dark field-STEM image with corresponding EDS mapping spectra from (h) to (k) (the scale bar is 50 nm)

Field emission scanning electron microscopy (FESEM) was utilized to explore the morphologies of different samples. Cross-sectional FESEM image in **Fig. S8a** shows that ZnO NWs grow vertically from FTO substrate with a thickness of *ca.* 1.5 μm and high-magnification FESEM image in **Fig.** S**8b** exhibits ZnO NWs with an average diameter of 40 nm. Panoramic FESEM image (**Fig. S8c**) shows that ZnO NWs substrate is virtually composed of nanowire with regular hexagonal cross-section and flat top surface. As reflected in **Fig. 3 (a** and **b)**, N-GQDs/ZnO NWs heterostructure (one assembly layer) exhibits much rougher surface than blank

ZnO NWs, indicating N-GQDs were uniformly coated on the ZnO NWs surface. Top-view FESEM image of N-GQDs/ZnO NWs heterostructure is analogous to blank ZnO NWs, implying the morphology of ZnO NWs was not altered with uniform deposition of N-GQDs.

Transmission electron microscopy (TEM) was used to verify the morphologies of the samples. As shown in **Fig. 3d** and **S9a**, pristine ZnO NWs exhibit a smooth surface which agrees with FESEM result. As revealed in the HRTEM image of ZnO NWs (**Fig. S9b**), lattice fringes were determined to be 0.28 and 0.26 nm, which are attributable to the (100) and $(0\bar{1}1)$ crystal planes of hexagonal wurtzite ZnO.[52] This indicates that ZnO NWs grow primarily along the (100) crystallographic plane which is in line with selected area electron diffraction (SAED) pattern result (inserted image in **Fig. S9b**). When N-GQDs were assembled on the ZnO NWs substrate, it was found that the morphology of N-GQDs/ZnO NWs heterostructure (**Fig. 3e**) is similar to pristine ZnO NWs other than the appearance of various black spots on the surface, which is due to the deposition of N-GQDs with small particle size (*ca.* 5.8 nm). Particularly, as displayed in **Fig. 3e** (inset), TEM image of a single nanowire apparently revealed rougher surface of N-GQDs/ZnO NWs heterostructure than blank ZnO NWs, indicating N-GQDs have indeed been closely attached to the surface of ZnO NWs afforded by LbL assembly. The components of N-GQDs and ZnO NWs in composite heterostructure can be ascertained by HRTEM image (**Fig. 3f**), and elemental mapping confirmed the coexistence of C and N on the ZnO NWs matrix in a homogeneous distribution (**Fig. 3 h-k**). In addition, uniform distribution of GQDs on the ZnO NWs can also be achieved by the same LbL assembly strategy (**Fig. S10**).

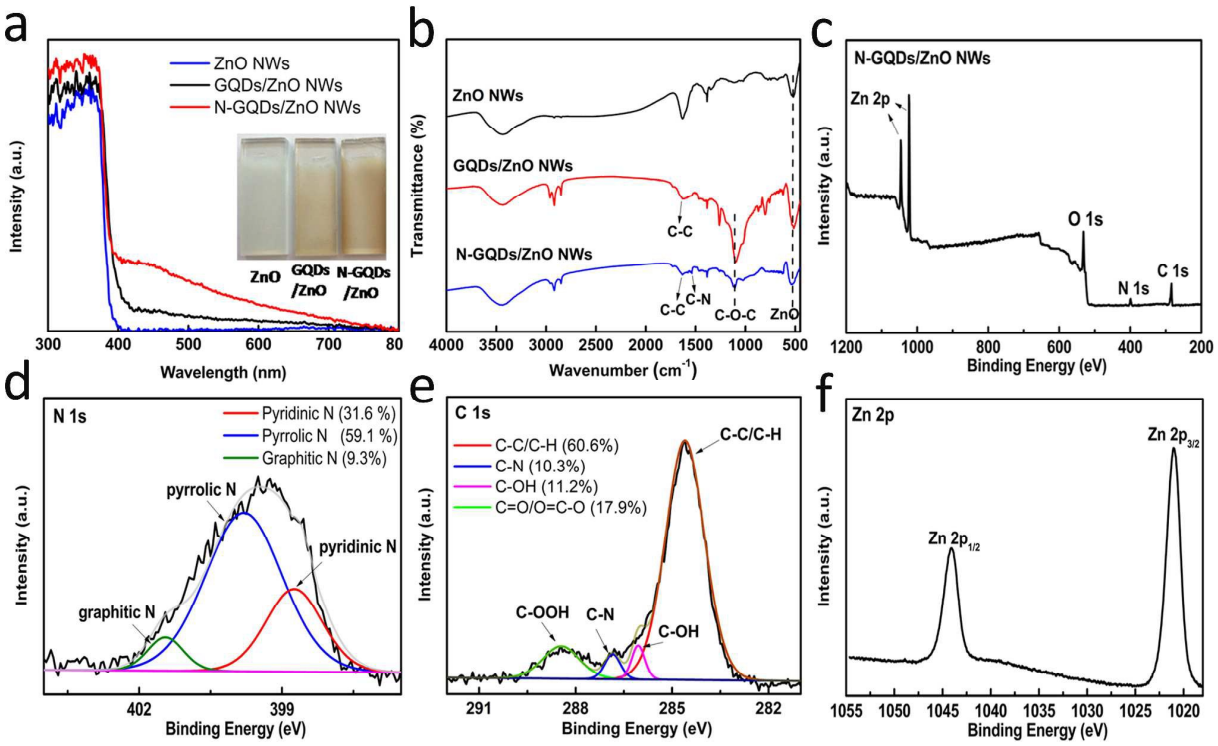

Fig. 4. (a) UV-vis diffuse reflectance spectra (DRS) and (b) FTIR spectra of ZnO NWs, GQDs/ZnO NWs (one assembly layer) and N-GQDs/ZnO NWs heterostructure (one assembly layer), (c) Survey XPS spectrum, and high-resolution (d) N 1s, (e) C 1s and (f) Zn 2p spectra of N-GQDs/ZnO NWs heterostructure (one assembly layer).

UV-vis diffuse reflectance spectra (DRS) were utilized to explore the optical properties of the samples. As displayed in **Fig. 4a**, a substantial absorption peak in UV region for different samples was observed which is ascribed to the bandgap excitation of ZnO. Moreover, it was found that, N-GQDs/ZnO NWs heterostructure with one assembly layer show distinct absorption band edge from blank ZnO NWs especially in visible region ranging from 400 nm to 800 nm. Notably, DRS result of ZnO NWs exhibits no absorption above 400 nm which agrees with bandgap of ZnO, while pronounced absorption in the same wavelength region was clearly seen for N-GQDs/ZnO NWs heterostructures, highlighting the pivotal role of N-GQDs as photo-sensitizers. Furthermore, it should be emphasized that N-GQDs/ZnO NWs heterostructures demonstrate significantly enhanced light absorption in visible region as compared with

GQDs/ZnO NWs counterpart with the same assembly layer, which highlights the contributing role of nitrogen doping in boosting light absorption of GQDs. In addition, as shown in **Fig. S11**, bandgap energies of different samples were roughly determined to be around 2.85, 2.90, and 3.18 eV corresponding to N-GQDs/ZnO NWs, GQDs/ZnO NWs and blank ZnO NWs, respectively. Therefore, DRS result suggests that uniform deposition of N-GQDs on ZnO NWs is beneficial for enhancing light harvest of ZnO NWs.

FTIR spectra were utilized to further unveil the structure of different samples. As displayed in **Fig. 4b** various carbonyl and carboxyl functional groups were observed in the FTIR spectrum of GQDs/ZnO NWs heterostructures. Apart from these peaks, a new peak at 1577 cm^{-1} corresponding to C-N groups of N-GQDs arose and, meanwhile, peak intensity of some other functional groups such as C-O-C stretching vibration mode at 1105.7 cm^{-1} and Zn-O group at 520 cm^{-1} concurrently decreased in the FTIR spectrum of N-GQDs/ZnO NWs heterostructure as compared with FTIR results of ZnO NWs and GQDs/ZnO NWs counterparts. The decreased intensity of these characteristic peaks suggests that interaction between N-GQDs and ZnO NWs is different from that between GQDs and ZnO NWs.

Survey XPS spectra of ZnO NWs, GQDs/ZnO NWs heterostructure, and N-GQDs/ZnO NWs heterostructure were performed, as displayed in **Fig. 4 (c-f)** & **S12**. Survey XPS spectrum of N-GQDs/ZnO NWs heterostructure mainly consists of C, N, O and Zn core-elements, indicating successful deposition of N-GQDs on the ZnO NWs. More specifically, as displayed in **Fig. 4** (**d** & **e**), high-resolution N 1s and C 1s spectra of N-GQDs/ZnO NWs heterostructure can be deconvoluted to several Gaussian peaks corresponding well to different types of functional groups, and the results are consistent with high-resolution N 1s and C 1s spectra of N-GQDs (**Fig. 1e** & **S5**). Furthermore, atomic ratio of C 1s to N 1s (C/N) in N-GQDs/ZnO NWs

heterostructure was determined to be *ca.* 13.8 %. Thus, the results indicate that N-GQDs have been successfully assembled on the ZnO NWs framework. In addition, high-resolution Zn 2p spectrum (**Fig. 4f**) for composite heterostructure shows binding energies of 1044.3 eV, and 1021.5 eV for Zn $2p_{1/2}$ and Zn $2p_{3/2}$, which unambiguously points to elemental chemical state of Zn^{2+} and suggests that the deposition of N-GQDs did not modify the chemical state of ZnO substrate.[21] **Fig. S13** shows the X-ray diffraction (XRD) patterns of different samples. Based on XRD result of ZnO NWs, six diffraction peaks including (100), (002), (001), (102), (110) and (103), were clearly identified, which correspond to wurtzite ZnO.[53] Moreover, it was found that diffraction peaks of ZnO were retained in the XRD pattern of N-GQDs (or GQDs)/ZnO NWs heterostructures, indicating N-GQDs (or GQDs) modification did not affect the crystalline structure of ZnO which is in line with HRTEM (**Fig. 3**) and XPS results (**Fig. 4**). Notably, no diffraction peaks of GQDs were observed in the composite nanostructures and this can be ascribed to low deposition amount of N-GQDs (or GQDs).

2.3. Photoelectrochemical water splitting performances

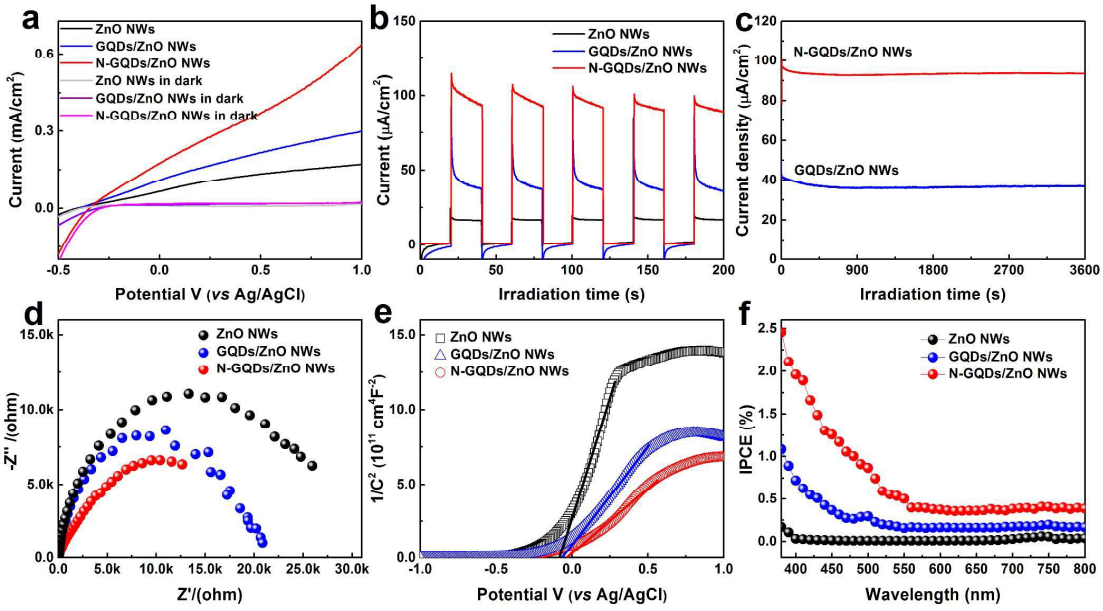

Fig. 5 (a) Current density *versus* applied voltage curves, (b) transient photocurrent responses of ZnO NWs, GQDs/ZnO NWs and N-GQDs/ZnO NWs heterostructures (using 1.0 mg/mL GQDs and N-GQDs aqueous solutions with one assembly layer), and (c) photostability of GQDs/ZnO NWs and N-GQDs/ZnO NWs heterostructures with zero bias *vs.* Ag/AgCl. (d) Electrochemical impedance spectroscopy Nyquist plots (amplitude of sinusoidal wave was set at 10 mV and frequency varied from 100 KHz to 0.1 Hz), (e) Mott-Schottky curves, and (f) Incident photon-to-current conversion efficiency (IPCE) spectra with zero bias *versus* Ag/AgCl of different samples. The PEC measurements were carried out in a 0.5 M Na_2SO_4 aqueous solution (pH = 7.34) under simulated solar light irradiation (100 mW cm^{-2}).

It is well-established that semiconductor's Fermi level in a PEC cell is equilibrated with the redox potential of electrolyte solution, which results in a band bending and generation of an electrical field.[54] Therefore, photogenerated minority charges carriers move from the semiconductor toward the interface between the semiconductor and electrolyte, by which water is either reduced to hydrogen with a p-type semiconductor (photocathode) or oxidized to oxygen by an n-type semiconductor (photoanode). In this regard, PEC water splitting reaction was utilized to evaluate the promising application of LbL-assembled N-GQDs/ZnO NWs heterostructure.

PEC water splitting performances of GQDs/ZnO NWs heterostructures with varied concentrations and assembly layers of GQDs were firstly systematically explored to determine the optimal experimental conditions in preparing N-GQDs/ZnO NWs heterostructures, as displayed in **Fig. S14** and **S15**. These results show that deposition amount of GQDs on ZnO NWs can be tuned by the concentration and assembly layer of GQDs during the LbL assembly process and the optimal concentration and assembly layer of GQDs were determined to be 1.0 mg/mL and one assembly layer. **Fig. 5a** demonstrates the photocurrent density as a function of applied bias voltage under simulated solar light irradiation (100 mW cm^{-2}), which shows that photocurrent density of different samples increases with the applied forward potential increasing, indicative of a typical n-type semiconductor.[55] It is obvious that N-GQDs/ZnO NWs

heterostructure (1.0 mg/mL N-GQDs with one assembly layer) exhibits dramatically enhanced photocurrent as compared with ZnO NWs and GQDs/ZnO NWs counterparts within the overall voltage profile. N-GQDs/ZnO NWs heterostructures with different assembly layers were also prepared by using diluted N-GQDs aqueous solutions (0.2 mg/ml) as the building block and PEC performances of which were also probed. The results showed that N-GQDs/ZnO NWs heterostructures with five assembly layers demonstrate the optimal photocurrent as compared with other counterparts (**Fig. S16**), but the value is still lower than that for the optimal sample fabricated by using 1.0 mg/mL N-GQDs. **Fig. 5b** records the periodic on/off transient photocurrent responses of different samples under intermittent simulated solar light irradiation. It is evident that the photocurrent of ZnO NWs was remarkably improved with uniform decoration of N-GQDs. In particular, N-GQDs/ZnO NWs heterostructure demonstrates almost five-fold and two-fold photocurrent enhancement in comparison with blank ZnO NWs and GQDs/ZnO NWs heterostructure, respectively. The superior photocurrent of N-GQDs/ZnO NWs heterostructures over other counterparts under the same experimental conditions suggests that photoexcited electron-hole pairs over N-GQDs/ZnO NWs heterostructures possess the most enhanced photosensitization efficiency. It was revealed that the photo-current density of N-GQDs-ZnO NWs composite prepared by a conventional coating method is much lower than that of LbL-assembled N-GQDs/ZnO NWs heterostructure (**Figure S17**). In addition, N-GQDs/ZnO NWs heterostructure demonstrates favorable photostability under continuous light irradiation and less than 3% of photocurrent decay was observed under irradiation for 1 h (**Fig. 5c)**. On a separate set of experiments when visible light (λ>420 nm) irradiation was used (**Fig. S18**), a similar photocurrent enhancement of N-GQDs/ZnO NWs heterostructure was also observed. More significantly and consistently, N-GQDs/TiO_2 nanorods (NRs) heterostructure (one assembly

layer) exhibit more significant photocurrent enhancement than GQDs/TiO_2 NRs and TiO_2 NRs under the same experimental conditions, following the order of: N-GQDs/TiO_2 NRs > GQDs/TiO_2 NRs > TiO_2 NRs (**Fig. S19** and **S20**). Consequently, based on the above analysis, an extraordinary photosensitization effect of N-GQDs on the PEC water splitting performances of LbL-assembled N-GQDs/1D semiconductor (ZnO NWs or TiO_2 NRs) heterostructures was unambiguously ascertained under both simulated solar and visible light irradiations.

To probe the separation efficiency of photogenerated charge carriers over N-GQDs/ZnO NWs heterostructure, electrochemical impedance spectroscopy (EIS) measurements of different samples under simulated solar light irradiation were performed (**Fig. 5d**).[56,57] The Nyquist plot from that of N-GQDs/ZnO NWs heterostructure exhibits the smallest semicircle radius than that of blank ZnO NWs and GQDs/ZnO NWs under light irradiation, indicating charge transfer resistance in the interface of ZnO NWs and electrolyte was reduced in the presence of N-GQDs, highlighting the key benefit of nitrogen doping in boosting charge transfer and hence the photocurrent generated. Mott-Schottky (M-S) plots are shown in **Fig. 5e**, in which slopes of the linear parts of all M-S plots are positive, indicative of typical n-type semiconductor property.[21] The linear parts of the M-S curves are extrapolated to $1/C^2 \rightarrow 0$ to estimate the Fermi level (U_{FL}) values of ZnO NWs, GQDs/ZnO NWs and N-GQDs/ZnO NWs heterostructures as -0.0855, -0.0581 and -0.0212 V (*vs* Ag/AgCl), respectively. The pronounced positive shift of U_{FL} for N-GQDs/ZnO NWs in comparison with ZnO NWs (36.9 mV *vs* Ag/AgCl) and GQDs/ZnO NWs (27.4 mV *vs* Ag/AgCl) suggests that modification of ZnO NWs with N-GQDs leads to a decrease in band bending edge, which is conducive to electron transfer from N-GQDs to ZnO under light irradiation. Consequently, M-S result indicates that N-GQDs/ZnO NWs heterostructure demonstrates the most enhanced charge transfer efficiency when compared with ZnO NWs and

GQDs/ZnO NWs counterparts, thus resulting in the significantly improved PEC water splitting performances. The carrier density (N_D) of different samples can be estimated by the following equation:[21]

$$N_D = (2 / e\varepsilon_0\varepsilon_r)[dU_{FL} / d(1 / C^2)]$$

where e = 1.6×10^{-19} C, $\varepsilon_0 = 8.86 \times 10^{-12}$ F m^{-1}, $\varepsilon_r = 8.12$ for wurtzite ZnO,[58] and C is the capacitance. The N_D values of ZnO, GQDs/ZnO NWs and N-GQDs/ZnO NWs heterostructure were determined to be 4.5×10^{18}, 1.02×10^{19} and 1.61×10^{19} cm^{-3}, respectively. The larger N_D value of N-GQDs/ZnO NWs heterostructure suggests more efficient charge transfer efficiency as compared with ZnO and GQDs/ZnO NWs counterparts and, thus, more significantly enhanced PEC water splitting performances.

Incident photon-to-current conversion efficiency (IPCE) spectra of different samples were further collected under monochromatic light irradiation as a function of incident light wavelength according to the following equation:[59]

$$IPCE = (1240I) / (\lambda J_{light})$$

where I is the photocurrent density, λ is the incident light wavelength, and J_{light} is the incident light intensity. As shown in **Fig. 5f**, N-GQDs/ZnO NWs heterostructure exhibits noticeable photoresponse in light region up to 800 nm, while ZnO NWs exhibit no photoresponse above 400 nm, which are in faithful agreement with DRS results. Compared with ZnO NWs based PEC cell, N-GQDs/ZnO NWs photoelectrode reveals an IPCE of *ca.* 0.86 % at a wavelength of 500 nm with zero applied voltage (*vs* Ag/AgCl), which is *ca.* 50 times and 3.0 times larger than those of blank ZnO NWs (0.017 %) and GQDs/ZnO NWs (0.29 %), respectively. Due to the negligible absorption at 500 nm for ZnO NWs, the clearly resolved peak in IPCE spectrum of N-

GQDs/ZnO NWs heterostructure can only be attributed to N-GQDs. Accordingly, IPCE results confirm that N-GQDs act as highly efficient photosensitizers and remarkably promote the light absorption of ZnO NWs in visible region, thereby giving rise to significantly enhanced PEC water-splitting performances of N-GQDs/ZnO NWs heterostructure.

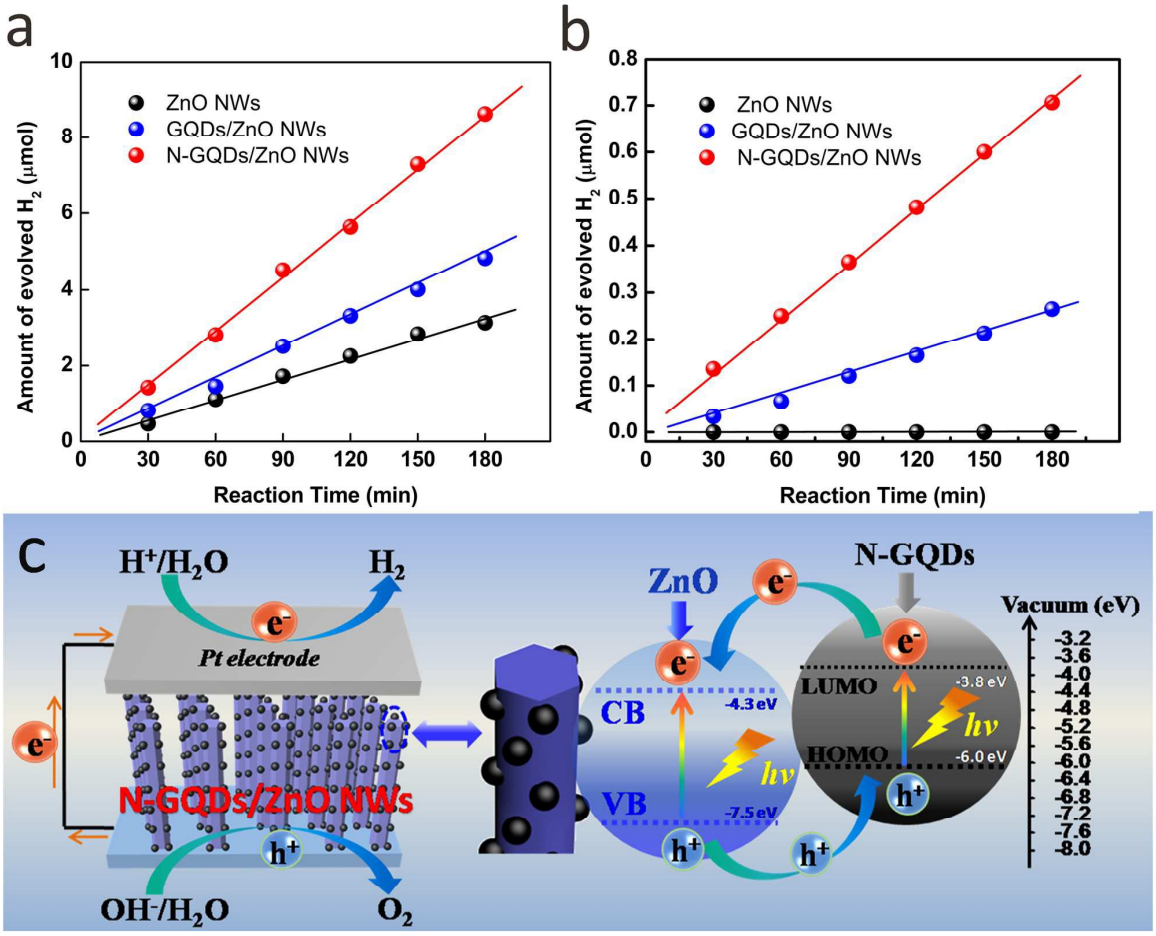

Fig. 6 Hydrogen evolution performances of ZnO NWs, GQDs/ZnO NWs and N-GQDs/ZnO NWs in 0.5 M Na_2SO_4 aqueous solution, (a) under simulated solar light irradiation (100 mW cm^{-2}), and (b) under visible light irradiation (> 420 nm). (c) Schematic illustration of PEC water splitting mechanism over N-GQDs/ZnO NWs heterostructure under simulated solar light irradiation.

To further evaluate the PEC performances of the different samples for hydrogen production, a gas-enclosed system with a gas chromatography under the same simulated solar or visible light irradiation was used to detect the amount of evolved gas. The amount of H_2 evolved over ZnO

NWs, GQDs/ZnO NWs, and N-GQDs/ZnO NWs under simulated solar light irradiation (100 mW cm^{-2}) for 180 min is shown in **Fig. 6a**, which indicates that the amount of H_2 generated almost increased linearly with the irradiation time, and the H_2 amount produced over N-GQDs/ZnO NWs heterostructure is nearly 4 and 2 times higher than those produced over blank ZnO NWs and GQDs/ZnO NWs, respectively, indicative of a synergistic contribution from nitrogen doping and photosensitization effect of GQDs in enhancing PEC hydrogen production performances of N-GQDs/ZnO NWs. Analogous results were observed under visible light irradiation over different samples, from which N-GQDs/ZnO NWs exhibits the largest hydrogen production amount in comparison with ZnO NWs and GQDs/ZnO NWs, as displayed in **Fig. 6b**. Therefore, consistent with PEC results which evidenced strong photocurrent enhancement, the current study strongly suggests that N-GQDs/ZnO NWs heterostructure can serve as an efficient electrode for hydrogen production under both simulated solar light and visible light irradiation.

The significant enhancement of hydrogen generation using the current N-GQDs/ZnO NWs heterostructure by proposing a PEC water splitting mechanism was illustrated in **Fig. 6c**. Based on Kohn-Sham molecular orbitals (MOs) theory, various electron transitions in N-GQDs can be triggered from the occupied levels (*i.e.*, Highest occupied molecular orbital, HOMO) to the unoccupied levels (*i.e.*, Lowest unoccupied molecular orbital, LUMO) under light irradiation, therefore endowing N-GQDs with a favorable HOMO-LUMO gap (**Fig. S21**) which acts like a semiconductor with small bandgap.[27,60] In this way, N-GQDs in our reaction system can be photoexcited under simulated solar, generating electron-hole pairs due to the favorable bandgap of N-GQDs/ZnO NWs heterostructure (2.85 eV, **Fig. S12**). In addition, considering the LUMO potential of N-GQDs (**Fig. S21d**) is more negative than the conduction band (CB) edge of ZnO,[27,60,61] and an intimate N-GQDs-to-ZnO NWs interfacial interaction resulted from the LbL

strategy, photoexcited electrons produced *in-situ* from N-GQDs under light irradiation can be spontaneously transferred to the CB of ZnO. Thus, photogenerated electrons and holes over N-GQDs are effectively separated and lifetime of the electron-hole charge carriers is significantly prolonged. Simultaneously, it should be noted that ZnO NWs substrate can also be photoexcited under simulated solar light irradiation in which electrons are excited from the valence band (VB) to the CB leaving holes in the VB. Under simulated solar light irradiation, both ZnO and N-GQDs were photoexcited giving rise to photogenerated charge carriers. The photogenerated holes on the valence band (VB) of ZnO can transfer to the HOMO of N-GQDs owing to their favorable band alignment and then oxide water to oxygen on the working electrode. Simultaneously, photoelectrons from LUMO of N-GQDs transfer to the CB of ZnO NWs and then to the external circuit producing photocurrent and ultimately reduce water to hydrogen on the counter electrode. When N-GQDs/ZnO NWs heterostructure was irradiated under visible light irradiation ($\lambda > 420$ nm), only N-GQDs can be photoexcited producing photoelectrons on the LUMO (**Fig S22**). Subsequently, the electrons transfer to the CB of ZnO and finally reduced water to hydrogen and the hole on the LUMO oxidize water to oxygen.

3. Conclusions

In summary, highly ordered N-GQDs decorated 1D semiconductor (ZnO NWs or TiO_2 NRs) nanohybrid heterostructures have been fabricated by a simple LbL assembly strategy based on pronounced electrostatic interaction. It was revealed that the well-defined LbL-assembled N-GQDs/ZnO NWs (as well as its N-GQDs/TiO_2 NRs counterpart) photoanode resulted in significantly enhanced PEC water splitting performances under both simulated solar and visible light irradiations, which is attributed to the extraordinary photosensitization effect of N-GQDs and intimate interfacial interaction between N-GQDs and ZnO NWs framework afforded by

nitrogen doping and LbL assembly. More significantly, PEC water splitting performances of N-GQDs/1D semiconductor heterostructures can be tuned by assembly layer. It is anticipated that our work could provide a general synthetic approach to prepare a large diversity of N-GQDs/semiconductor nanoarchitectures and afford new insights for the potential applications of N-GQDs in the field of photocatalysis, photoelectrocatalysis and photoelectrochemical systems.

Experiment Section

Synthesis of graphene oxide quantum dots (GQDs)

Graphene oxide quantum dots (GQDs) were synthesized with CX-72 carbon black via being refluxed in a concentrated nitric acid (HNO_3) solution.[34,62] Typically, 0.4 g dried CX-72 carbon black was added to 6 mol L-1 nitric acid (100 mL) and refluxed for 24 h at 110 ºC. After cooling to below 30 ºC, the product was centrifuged (12000 rpm) for 10 min to achieve sediment and a supernatant. The resulting supernatant was treated at 200 ºC to evaporate the nitric acid and water. After cooling to room temperature, a reddish-brown solid was acquired. Finally, GQDs aqueous solution was obtained by dissolving GQDs in DI H_2O under 10 min sonication.

Synthesis of nitrogen-doped graphene oxide quantum dots (N-GQDs)

N-GQDs was prepared by using GQDs and ammonium nitrate as precursors.[48] 100 mg GQDs and 100 mg ammonium nitrate were dissolved in 10 mL of ethanol and the mixed solution was stirred for 20 min. Then, the solution temperature was increased to 60 ºC to evaporate ethanol whilst stirring. After that, the dried mixture was put into a furnace for calcination at 350 ºC for 1.5 h at a heating rate of 5 ºC/min. Finally, the sample was dissolved in DI H_2O under 30 min sonication and dialyzed (MWCO, 12-14 KD, Spectra/Por) for 3 days to remove residual ammonium and nitrate ions, and dried in an over at 100 ºC for 12 h.

Synthesis of ZnO NWs and TiO_2 NRs

Fluorine-doped tin oxide (FTO) substrates were cleaned in a freshly prepared piranha solution (3:1 concentrated 98% H_2SO_4/30% H_2O_2) for 30 min, rinsed with DI H_2O, and dried with a gentle stream of N_2. 110 mg zinc acetate was added to ethanol solution to obtain 5 mM zinc acetate solution. 5-8 drops of the prepared zinc acetate solution was then dropped onto the FTO substrate with conducting layer facing up. After about 25 s, the piece of FTO was rinsed in pure ethanol solution and immediately taken out and put in an electric oven at 100 ºC for drying. This process was repeated for 4 times, and thus the FTO with ZnO seeds was obtained by calcinating at 350 ºC in air for 30 min.

The growth solution was prepared by adding 100 mL of 0.05 M of methenamine into 100 mL of 0.05 M zinc nitrate solution. A piece of FTO coated with ZnO seeds was immersed into the growth solution, containing 25 mM $Zn(NO_3)_2$ and 25 mM methenamine and kept in an electric oven at 95 ºC for 3 h. Finally, the as-prepared ZnO NWs were calcinated at 400 ºC in air for 1 h.

TiO_2 nanorod arrays (TiO_2 NRs) on FTO substrate were prepared by a hydrothermal method based on our previous work.[63,64] Typically, FTO substrates were cleaned in a freshly prepared piranha solution (3:1 concentrated 98% H_2SO_4/30% H_2O_2) for 30 min, rinsed with DI H_2O, and dried with a gentle stream of N_2. The precursor was synthesized by adding 0.45 mL of titanium butoxide (97 %, Aldrich) to a solution containing HCl (15 mL) and DI H_2O (15 mL), and then the mixture was stirred for 10 min until the solution became clear. Then, the precursor solution was poured into a Teflon-liner stainless autoclave (50 mL) with the FTO substrates placed at an angle against the wall with the conductive side facing down. Hydrothermal method was conducted at 150 ºC for 12 h in an oven. Afterwards, the FTO substrate were rinsed with DI H_2O and dried in ambient air.

LbL assembly of N-GQDs/ZnO NWs (N-GQDs/TiO_2 NRs) and GQDs/ZnO NWs (GQDs/TiO_2 NRs) heterostructures

The detailed assembly procedure is illustrated in **Scheme 1**. ZnO NWs substrate was firstly dipped into polyethylenimine (PEI) aqueous solution (1.0 mg/mL, 0.5 M NaCl, pH=7.23) for 10 min and washed three times with DI H_2O, followed by drying with a gentle stream of N_2. Subsequently, the resultant substrate was immersed in N-GQDs or GQDs aqueous suspension (1.0 mg/mL, pH=6.89) for 10 min, rinsed with DI H_2O, and dried by a stream of N_2. The above procedure as a whole was designated as a single assembly layer. Multilayered deposition of N-GQDs or GQDs on ZnO NWs was achieved by repeating the dipping cycle. It should be pointed out that different concentrations (from 0.2 to 1.5 mg/mL,) and different assembly layers (from 1 to 20 layers,) of GQDs were utilized in fabricating GQDs/ZnO NWs heterostructures, and the results indicate that the optimal parameter is 1.0 mg/mL GQDs aqueous suspension with one assembly layer. Thus, N-GQDs aqueous suspension was prepared based on 1.0 mg/mL GQDs aqueous solution and one assembly layer of N-GQDs was deposited on the ZnO NWs. Finally, the LbL-assembled N-GQDs/ZnO and GQDs/ZnO NWs heterostructures were calcined in an argon atmosphere at 400 ^oC for 1 h at a heating rate of 5 ^oC/min. GQDs/TiO_2 NRs and N-GQDs/TiO_2 NRs heterostructures were fabricated with similar method as mentioned above.

PEC water splitting performances measurements

PEC water splitting measurements were carried out in a homemade three-electrode quartz cell with electrochemical workstation (CHI 66D) in which platinum sheet was employed as counter electrode and Ag/AgCl electrode as reference electrode, and the samples with an active area of 15.9 mm^2, provided by a mask with a diameter of 4.5 mm, was used as the working electrodes. Aqueous Na_2SO_4 solution (0.5 M) was used as the electrolyte. The light source (100 mW cm^{-2})

was provided by a 300 W Xenon arc lamp with an AM 1.5 G filter (Newport) and a UV cutoff filter ($\lambda > 420$ nm). The incident photon-to-current conversion efficiency (IPCE) spectra of the samples were measured by using monochromatic light, which is carried out with a Xenon light illuminated under a Cornerstone monochromator. The signal of photocurrent was collected by a Merlin lock-in radiometry with reference to a calibrated silicon diode. The amount of evolved gas was detected by a gas chromatograph (Agilent 7890A GC with TCD detector; carrier gas: ultra-high-purity nitrogen). Typically, a inflow of N_2 was continuously bubbled into the electrolyte (0.5 M Na_2SO_4 solution) for half hour 30 min to remove traces of O_2 and H_2 in the gas collection system. During the measurement of gaseous product, the simulated solar light source (or visible light source) was provided by a 150 W Xenon arc lamp with an AM 1.5 G filter (or a UV cutoff filter ($\lambda > 420$ nm), Newport), and the gas was manually injected into GC at an interval of 30 min.

Conflict of Interest: The authors declare no competing financial interest.

Acknowledgements. This work was supported by the Nanyang Technological University Start-up Grant (M4081326).

Supporting Information Available: Characterization of GQDs and N-GQDs. TEM, and AFM image of GQDs, Survey and high-resolution C 1s and O 1s spectra of GQDs. UV-vis absorption spectrum and PL spectra of GQDs aqueous suspension. FTIR, and Raman spectra of GQDs and N-GQDs. Survey and high resolution C 1s spectra of N-GQDs. Zeta potentials of GQDs and N-GQDs aqueous suspensions as a function of pH value. Molecular structure of polyethylenimine (PEI, $(C_2H_5N)_n$). Characterization of ZnO NWs, GQDs/ZnO NWs. Cross-sectional FESEM images of GQDs/ZnO NWs heterostructure (one assembly layer), TEM and HRTEM images of GQDs/ZnO NWs heterostructure. High-resolution C 1s, (b) O 1s and Zn 2p spectra of ZnO NWs.

High-resolution C 1s, O 1s and Zn 2p spectra of GQDs/ZnO NWs heterostructure (one assembly layer). The plot of transformed Kubelka-Munk function *versus* the energy of light of ZnO NWs, GQDs/ZnO NWs and N-GQDs/ZnO NWs heterostructures. Control experiment with different concentrations and assembly layers of GQDs for PEC performances. UV-vis diffuse reflectance spectra (DRS) and light-responsive linear-sweep voltammograms (LSV) curves of GQDs/ZnO NWs heterostructures fabricated with different concentrations and assembly layers of GQDs. LSV curves, transient photocurrent responses of ZnO NWs, GQDs/ZnO NWs (one assembly layer) and N-GQDs/ZnO NWs (one assembly layer), and photostability of GQDs/ZnO NWs and N-GQDs/ZnO NWs heterostructures under visible light irradiation ($\lambda > 420$ nm). LSV curves, transient photocurrent responses of TiO_2 NRs, GQDs/TiO_2 NRs (one assembly layer) and N-GQDs/TiO_2 NRs (one assembly layer) under simulated solar and visible light irradiation ($\lambda > 420$ nm).

References

1 H. B. Yang, J. Miao, S. F. Hung, F. Huo, H. M. Chen and B. Liu, *ACS Nano,* 2014, **8**, 10403-10413.
2 Z. Li, W. Luo, M. Zhang, J. Feng and Z. Zou, *Energ. Environ. Sci.,* 2013, **6**, 347-370.
3 M. G. Walter, E. L. Warren, J. R. McKone, S. W. Boettcher, Q. Mi, E. A. Santori and N. S. Lewis, *Chem. Rev.* 2010, **110**, 6446-6473.
4 N. S. Lewis and D. G. Nocera, *Proc. Natl. Acad. Sci.,* 2006, **103**, 15729-15735.
5 Y. H. Ng, S. Ikeda, M. Matsumura and R. Amal, *Energ. Environ. Sci.,* 2012, **5**, 9307-9318.
6 K. Iwashina, A. Iwase, Y. H. Ng, R. Amal and A. Kudo, *J. Am. Chem. Soc.,* 2015, **137**, 604-607.
7 A. Fujishima and K. Honda, *Nature* 1972, **238**, 37-38.
8 Y. Qiu, K. Yan, H. Deng and S. Yang, *Nano Lett.,* 2012, **12**, 407-413.
9 Y. Lin, Y. Xu, M. T. Mayer, Z. I. Simpson, G. McMahon, S. Zhou and D. Wang, *J. Am. Chem. Soc.* 2012, **134**, 5508-5511.
10 S. Liu, Z. R. Tang, Y. Sun, J. C. Colmenares and Y. J. Xu, *Chem. Soc. Rev.* 2015, **44**, 5053-5057.
11 F. X. Xiao, J. Miao, H. Tao, S. F. Hung, H. Y. Wang, H. B. Yang, J. Chen, R. Chen and B. Liu, *Small* 2015, **11**, 2115-2131.
12 H. M. Chen, C. K. Chen, Y. C. Chang, C. W. Tsai, R. S. Liu, S. F. Hu, W. S. Chang and K. H. Chen, *Angew. Chem. Int. Edit.* 2010, **122**, 6102-6105.
13 F. X. Xiao, S. F. Hung, H. Tao, J. Miao, H. B. Yang and B. Liu, *Nanoscale* 2014, **6**, 14950-14961.
14 G. Wang, H. Wang, Y. Ling, Y. Tang, X. Yang, R. C. Fitzmorris, C. Wang, J. Zhang and Y. Li, *Nano Lett.,* 2011, **11**, 3026-3033.
15 Y. G. Lin, Y. K. Hsu, Y. C. Chen, S. B. Wang, J. T. Miller, L. C. Chen and K. H. Chen, *Energ. Environ. Sci.,* 2012, **5**, 8917-8922.
16 H. M. Chen, C. K. Chen, M. L. Tseng, P. C. Wu, C. M. Chang, L. C. Cheng, H. W. Huang, T. S. Chan, D. W. Huang, R. S. Liu and D. P. Tsai, *Small,* 2013, **9**, 2926-2936.
17 P. Thiyagarajan, H. J. Ahn, J. S. Lee, J. C. Yoon and J. H. Jang, *Small,* 2013, **9**, 2341-2347.
18 V. Subramanian, E. E. Wolf and P. V. Kamat, *J. Phys. Chem. B,* 2003, **107**, 7479-7485.
19 Y. G. Lin, Y. K. Hsu, Y. C. Chen, L. C. Chen, S. Y. Chen and K. H. Chen, *Nanoscale,* 2012, **4**, 6515-6519.
20 S. Xie, X. Lu, T. Zhai, W. Li, M. Yu, C. Liang and Y. Tong, *J. Mater. Chem.,* 2012, **22**, 14272-14275.
21 X. Yang, A. Wolcott, G. Wang, A. Sobo, R. C. Fitzmorris, F. Qian, J. Z. Zhang and Y. Li, *Nano Lett.* 2009, **9**, 2331-2336.
22 H. X. Li, C. W. Cheng, X. L. Li, J. P. Liu, C. Guan, Y. Y. Tay and H. J. Fan, *J. Phys. Chem. C,* 2012, **116**, 3802-3807.
23 J. Miao, H. B. Yang, S. Y. Khoo and B. Liu, *Nanoscale,* 2013, **5**, 11118-11124.
24 Z. Yin, Z. Wang, Y. Du, X. Qi, Y. Huang, C. Xue and H. Zhang, *Adv. Mater.,* 2012, **24**, 5374-5378.
25 L. A. Ponomarenko, F. Schedin, M. I. Katsnelson, R. Yang, E. W. Hill, K. S. Novoselov and A. K. Geim, *Science,* 2008, **320**, 356-358.
26 J. Lu, P. S. E. Yeo, C. K. Gan, P. Wu and K. P. Loh, *Nat. Nanotechnol.,* 2011, **6**, 247-252.
27 T. F. Yeh, C. Y. Teng, S. Chen and H. Teng, *Adv Mater,* 2014, **26**, 3297-3303.
28 H. Cheng, Y. Zhao, Y. Fan, X. Xie, L. Qu and G. Shi, *ACS Nano,* 2012, **6**, 2237-2244.

29 Z. Zhang, J. Zhang, N. Chen and L. Qu, *Energ. Environ. Sci.,* 2012, **5**, 8869-8890.
30 J. Peng, W. Gao, B. K. Gupta, Z. Liu, R. Romero-Aburto, L. H. Ge, L. Song, L. B. Alemany, X. B. Zhan, G. H. Gao, S. A. Vithayathil, B. A. Kaipparettu, A. A. Marti, T. Hayashi, J. J. Zhu and P. M. Ajayan, *Nano Lett.,* 2012, **12**, 844-849.
31 R. Liu, D. Wu, X. Feng and K. Mullen, *J. Am. Chem. Soc.,* 2011, **133**, 15221-15223.
32 X. Yan, X. Cui, B. Li and L. Li, *Nano Lett.,* 2010, **10**, 1869-1873.
33 N. Zhang, M. Q. Yang, S. Liu, Y. Sun and Y. J. Xu, *Chem. Rev.,* 2015, **115**, 10307-10377.
34 C. X. Guo, Y. Dong, H. B. Yang and C. M. Li, *Adv. Energy Mater.,* 2013, **3**, 997-1003.
35 Y. Xue, J. Liu, H. Chen, R. Wang, D. Li, J. Qu and L. Dai, *Angew. Chem. Int. Edit.,* 2012, **51**, 12124-12127.
36 T. Susi, J. Kotakoski, R. Arenal, S. Kurasch, H. Jiang, V. Skakalova, O. Stephan, A. V. Krasheninnikov, E. I. Kauppinen, U. Kaiser and J. C. Meyer, *ACS Nano,* 2012, **6**, 8837-8846.
37 C. Mattevi, G. Eda, S. Agnoli, S. Miller, K. A. Mkhoyan, O. Celik, D. Mastrogiovanni, G. Granozzi, E. Garfunkel and M. Chhowalla, *Adv. Funct. Mater.,* 2009, **19**, 2577-2583.
38 X. Zhou, L. J. Wan and Y. G. Guo, *Adv. Mater.,* 2013, **25**, 2152-2157.
39 D. Yu, E. Nagelli, F. Du and L. M. Dai, *J. Phys. Chem. Lett.,* 2010, **1**, 2165-2173.
40 G. Decher, *Science,* 1997, **277**, 1232-1237.
41 F. X. Xiao, Z. Zeng and B. Liu, *J. Am. Chem. Soc.,* 2015, **137**, 10735-10744.
42 F. X. Xiao, J. Miao and B. Liu, *J. Am. Chem. Soc.,* 2014, **136**, 1559-1569.
43 Q. Tang, J. Wu, Q. Li and J. Lin, *Polymer,* 2008, **49**, 5329-5335.
44 S. Zhu, J. Zhang, S. Tang, C. Qiao, L. Wang, H. Wang, X. Liu, B. Li, Y. Li, W. Yu, X. Wang, H. Sun and B. Yang, *Adv. Funct. Mater.,* 2012, **22**, 4732-4740.
45 D. Qu, M. Zheng, L. Zhang, H. Zhao, Z. Xie, X. Jing, R. E. Haddad, H. Fan and Z. Sun, *Sci. Rep.,* 2014, **4**, 5294.
46 Y. Zheng, Y. Jiao, L. Ge, M. Jaroniec and S. Z. Qiao, *Angew. Chem. Int. Edit.,* 2013, **52**, 3192-3198.
47 S. Wang, L. Zhang, Z. Xia, A. Roy, D. W. Chang, J. B. Baek and L. Dai, *Angew. Chem. Int. Edit.,* 2012, **51**, 4209-4212.
48 H. Sun, Y. Wang, S. Liu, L. Ge, L. Wang, Z. Zhu and S. Wang, *Chem. Commun.,* 2013, **49**, 9914-9916.
49 C. Wang, Y. Zhou, L. He, T. W. Ng, G. Hong, Q. H. Wu, F. Gao, C. S. Lee and W. Zhang, *Nanoscale,* 2013, **5**, 600-605.
50 N. A. Kumar, H. Nolan, N. McEvoy, E. Rezvani, R. L. Doyle, M. E. G. Lyons and G. S. Duesberg, *J. Mater. Chem. A,* 2013, **1**, 4431-4435.
51 P. L. Kuo and W. F. Chen, *J. Phys. Chem. B,* 2003, **107**, 11267-11272.
52 W. Wang, L. Wang, L. Liu, C. He, J. Tan and Y. Liang, *Crystengcomm.,* 2012, **14**, 4997-5004.
53 P. Yang, H. Yan, S. Mao, R. Russo, J. Johnson, R. Saykally, N. Morris, J. Pham, R. He and H. J. Choi, *Adv. Funct. Mater.,* 2002, **12**, 323-331.
54 F. X. Xiao, S. F.Hung, J. Miao, H. Wang, H. B. Yang and B. Liu, *Small,* 2015, **11**, 554-567.
55 M. J. Natan, J. W. Thackeray and M. S. Wrighton, *J. Phy. Chem.,* 1986, **90**, 4089-4098.
56 N. Li, G. Liu, C. Zhen, F. Li, L. Zhang and H. M. Cheng, *Adv. Funct. Mater.,* 2011, **21**, 1717-1722.
57 Z. Zhang, L. Zhang, M. N. Hedhili, H. Zhang and P. Wang, *Nano Lett.,* 2013, **13**, 14-20.
58 Z. Zhan, Y. Wang, Z. Lin, J. Zhang and F. Huang, *Chem. Commun.,* 2011, **47**, 4517-4519.

59 A. Wolcott, W. A. Smith, T. R. Kuykendall, Y. Zhao and J. Z. Zhang, *Adv. Funct. Mater.,* 2009, **19**, 1849-1856.
60 L. Tang, R. Ji, X. Li, K. S. Teng and S. P. Lau, *J. Mater. Chem. C*, 2013, **1**, 4908-4915.
61 M. H. Huang, S. Mao, H. Feick, H. Yan, Y. Wu, H. Kind, E. Weber, R. Russo and P. Yang, *Science,* 2001, **292**, 1897-1899.
62 Z. Zeng, D. Yu, Z. He, J. Liu, F. X. Xiao, Y. Zhang, R. Wang, D. Bhattacharyya and T. T. Y. Tan, *Sci. Rep.,* 2016, **6**, 20142.
63 B. Liu and E. S. Aydil, *J. Am. Chem. Soc.,* 2009, **131**, 3985-3990.
64 F. X. Xiao, J. Miao and B. Liu, *Mater. Horizons,* 2014, **1**, 259-263.